In-situ observation of stacking fault evolution in vacuum-deposited C_{60}

J. F. M. Hardigree, I. R. Ramirez, G. Mazzotta, C. Nicklin, and M. Riede

Citation: Appl. Phys. Lett. **111**, 233305 (2017);
View online: https://doi.org/10.1063/1.4995571
View Table of Contents: http://aip.scitation.org/toc/apl/111/23
Published by the American Institute of Physics

Articles you may be interested in

Understanding the grain-growth mechanism of high-performance organic semiconducting diphenyl-dibenzothiopheno[6,5-b:6′,5′-f]thieno[3,2-b]thiophene molecules
Applied Physics Letters **111**, 233301 (2017); 10.1063/1.4999966

Temperature-dependent electronic properties of inorganic-organic hybrid halide perovskite ($CH_3NH_3PbBr_3$) single crystal
Applied Physics Letters **111**, 233302 (2017); 10.1063/1.5005005

Comparative study of organic transistors with different graphene electrodes fabricated using a simple patterning method
Applied Physics Letters **111**, 233303 (2017); 10.1063/1.4997780

Low turn-on voltage perovskite light-emitting diodes with methanol treated PEDOT:PSS as hole transport layer
Applied Physics Letters **111**, 233304 (2017); 10.1063/1.5010245

Charge carrier velocity in graphene field-effect transistors
Applied Physics Letters **111**, 233505 (2017); 10.1063/1.5003684

MINERVA: A facility to study Microstructure and INterface Evolution in Realtime under VAcuum
Review of Scientific Instruments **88**, 103901 (2017); 10.1063/1.4989761

In-situ observation of stacking fault evolution in vacuum-deposited C_{60}

J. F. M. Hardigree,[1,a)] I. R. Ramirez,[1] G. Mazzotta,[1] C. Nicklin,[2] and M. Riede[1]
[1]*Clarendon Laboratory, Department of Physics, University of Oxford, Oxfordshire OX1 3PU, United Kingdom*
[2]*Diamond Light Source, Didcot, Oxfordshire OX11 0DE, United Kingdom*

(Received 12 July 2017; accepted 13 November 2017; published online 8 December 2017)

We report an *in-situ* study of stacking fault evolution in C_{60} thin films using grazing-incidence x-ray scattering. A Williamson-Hall analysis of the main scattering features during growth of a 15 nm film on glass indicates lattice strain as high as 6% in the first 5 nm of the film, with a decrease to 2% beyond 8 nm thickness. Deformation stacking faults along the {220} plane are found to occur with 68% probability and closely linked to the formation of a nanocrystalline powder-like film. Our findings, which capture monolayer-resolution growth, are consistent with previous work on crystalline and powder C_{60} films, and provide a crystallographic context for the real-time study of organic semiconductor thin films. © *2017 Author(s). All article content, except where otherwise noted, is licensed under a Creative Commons Attribution (CC BY) license (http://creativecommons.org/licenses/by/4.0/).* https://doi.org/10.1063/1.4995571

The structure of small-molecule organic semiconductors in thin film electronic devices has been the subject of numerous studies, stimulated by the interest in developing low-cost electronic devices for health monitors,[1,2] displays,[3] solar cells,[4] and digital logic[5,6] from simple organic building blocks. Thin films of small-molecule organic semiconductors can exhibit a wide range of microstructural motifs, which are intimately linked to properties as diverse as absorption,[7,8] photogenerated exciton diffusion,[9,10] photoluminsescence,[11] charge carrier mobility,[12–14] and analyte gas diffusivity.[15,16] *In-situ* techniques that enable real-time monitoring of vacuum-deposited thin films can provide highly granular spatio-temporal information for probing the underlying physics of organic film formation[17–20] and help elucidate the generalisable processing-structure-property relationships sought for advanced device fabrication.

The molecular and thin film structure of C_{60} fullerene, a ubiquitous organic semiconductor, has been investigated in detail since its successful synthesis nearly 30 years ago.[21] Among the many mesoscale features of C_{60} solids are a high density of twins and stacking faults along the ⟨111⟩ close-packing direction, attributed to the weak van der Waals interactions between fullerenes.[22–24] Stacking faults are a feature of materials with face-centered cubic (FCC) structures, in which several sets of tetrahedral positions are available in a given ⟨111⟩ plane. While FCC stacking consists of planes following a 3-plane sequence of alternating tetrahedral positions (A-B-C-A-B-C), a stacking fault occurs when atoms in the third plane in this sequence occupy tetrahedral positions corresponding to those of the A planes. A particular type of stacking fault known as crystal twinning occurs when the fourth plane takes the position of a B plane instead (*e.g.*, A-B-C-B-A). Such faults disrupt translational symmetry along the close packed ⟨111⟩ direction, impacting macroscopic properties such as charge transport through the formation of gap states and interfacial energy barriers in inorganic semiconductor thin films.[25] Although studies of bulk crystalline[23] and vacuum-deposited thin film[26,27] C_{60} have identified the presence of stacking faults and twins, there has been much less work aimed at quantifying these and probing how they evolve during deposition, especially under industrially relevant processing conditions.

To investigate the evolution of C_{60}, we employed a recently developed multi-source deposition chamber at the Diamond Light Source that enables grazing-incidence X-ray scattering (GIXS) measurements of growing molecular thin films during thermal deposition.[28] Capturing the growth dynamics of organic molecular films at industrially relevant deposition rates (0.1–1 Å/s)[29] presents various technical challenges. The low scattering density of organic materials necessitates longer exposure times than that of films of a similar thickness of high-Z atomic species to achieve similar contrast.[30] It is also established that organic thin films—in particular samples less than 10 nm thick—are susceptible to x-ray beam damage.[30,31] Consequently, tracking the scattering of the growing film requires balancing the deposition rate and x-ray exposure time, such that each image provides a sufficiently discrete snapshot of the film's current state without subjecting it to detrimental beam damage that could influence subsequent layers. To balance these competing needs, we set a fullerene evaporation rate of 0.1 Å/s (∼1 monolayer/min) and used a 10 s exposure time on a 2D detector (Pilatus 2M). To limit the beam exposure, we spaced measurements by 65 s [Fig. S1(a) in the supplementary material]. Because the angle of incidence during *in-situ* measurements was set to 0.072°, the minimum x-ray penetration depth is $z_{1/e,min} = (2\sqrt{r_e}\pi\rho)^{-1} = 7.5$ nm in C_{60}.[32,33] As a result, the images obtained during the first 7.5 nm capture the accumulating growing film on the substrate, while images acquired at greater thickness capture the upper 7.5 nm of the film. Images were calibrated using silver behenate (AgBeh), and data reduction was performed using *DAWN*;[34] further details on sample preparation and alignment procedures can be found in the supplementary material and in a separate report with the technical details of the deposition chamber.[28]

[a)]Author to whom correspondence should be addressed: josue.martinez-hardigree@physics.ox.ac.uk

 © Author(s) 2017.

During the initial few nm of growth, we observe the nucleation of C_{60} crystallites on the glass surface, as revealed by the rapid changes in the diffuse scatter captured in the images of Figs. 1(a)–1(d). The convergence of the broad scattering near $q_z = 0.15\,\text{Å}^{-1}$ towards $q_z = 0.138\,\text{Å}^{-1}$ in the first 300 s or 3 nm of growth is consistent with the complete coverage of the surface with ~4 monolayers of C_{60}. By monitoring the parallel scattering q_{xy} over the first 300 s in Fig. 1(e), an estimate of the distance between island centers[35] can be extracted from the peak position of the diffuse scatter, with the correlation length $D_{diffuse} \approx 2\pi/\Delta q_{xy}$. Features appear near $q_{xy} = 0.02\,\text{Å}^{-1}$ after depositing just under 1 nm of C_{60} (~1 monolayer), consistent with an island-island spacing of 29.1 nm. The tapering of $D_{diffuse}$ to a constant value of 45 nm after 8 nm thickness reflects that the film has reached steady-state growth and coincides with the expected penetration depth of x-rays at this energy and angle of incidence. This value is consistent with 47.69 nm found from the FFT analysis of atomic force microscopy (AFM) of a 15 nm C_{60} film (Fig. S4 in the supplementary material).

Simple reflectivity models with constant roughness $\sigma_{C60/air} = 0.2$ nm for the C_{60} layer and glass roughness $\sigma_{glass/C60} = 1.0$ nm (Fig. S2 in the supplementary material) are only able to match the oscillation period obtained at $\mathbf{q_z} = 0.138\,\text{Å}^{-1}$, but a full description of the measured off-specular reflectivity using an adjustment of the model by Woll *et al.*[18,19] is required to fully capture the growth behavior of the film. As a consequence, the reported film thickness is based on the response of a calibrated quartz crystal monitor (QCM) within the deposition chamber[28] and does not account for changes in thickness which may arise from differences in the sticking coefficient of C_{60} at room temperature within the first few layers of the film. For a comprehensive investigation of the sticking coefficient and thermally assisted dewetting of C_{60} and its implications on observed film growth, the reader is referred to a recent study that makes use of *in-situ* x-ray reflectivity to quantify dewetting and upward mass transport by monitoring the specular signal from film deposition up to 60 min post-deposition.[36]

Complementary in-plane scattering along the substrate horizon ($q_z = 0.022\,\text{Å}^{-1}$) affords insights into the crystallographic evolution of the upper 7.5 nm of the growing film. Reflections from background-subtracted images (details in supplementary material) were fitted to Gaussian peaks using open-source software tools.[37,38] As shown in Fig. 2(b), the {111} reflection ($q_{xy} = 0.8\,\text{Å}^{-1}$) appears after the first nanometer of growth, indicating that the surface is populated by hexagonally close packed islands of C_{60}. Initially, the features near $q_{xy} = 1.3\,\text{Å}^{-1}$ and $1.4\,\text{Å}^{-1}$ are indistinguishable from a broad scattering area, but within the first 4 nm, these features quickly become more readily distinguishable from one another, and their peak widths begin to narrow consistent with domain growth. During the first 5 nm of growth, we observe a marked transition from near the $\{310\}_{FCC}$ plane to a value between the $\{311\}_{FCC}$ plane and the $\{021\}_{HCP}$ plane. Simultaneously, the feature near $1.3\,\text{Å}^{-1}$ initially appears near the $\{221\}_{FCC}$ plane but with increasing thickness converges towards a q value between that of the $\{220\}_{FCC}$ and $\{111\}_{HCP}$ planes. These shifts of the scattering vector for both features to intermediate

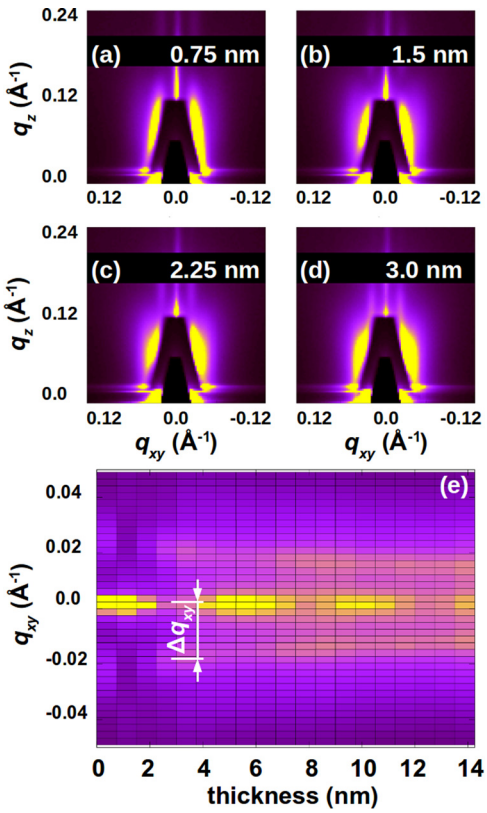

FIG. 1. Grazing-incidence x-ray scattering (GIXS) images during nucleation and growth on glass. (a)–(d) Detector images in the small angle region near the beamstop. The black band in the images corresponds to intermodular gap on the Pilatus detector. (e) Diffuse scatter as a function of film thickness measured in the region denoted by the white box ($q_z = 0.138\,\text{Å}^{-1}$) indicated in (a).

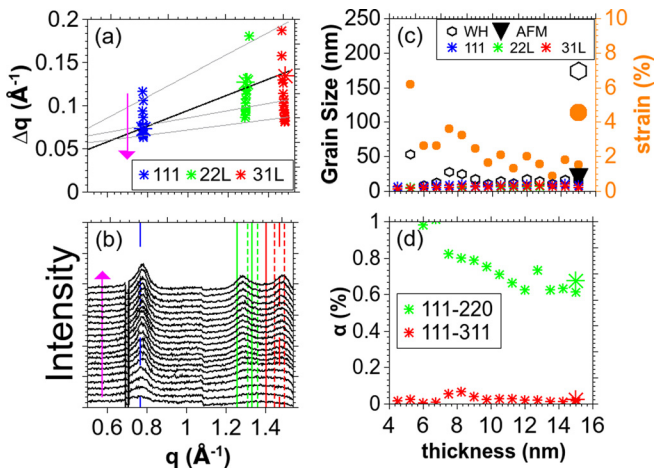

FIG. 2. Comparison of scattering features observed in the GIXS measurements at $q_z = 0.022\,\text{Å}^{-1}$. (a) Williamson-Hall (WH) plot of Δq vs q for thickness starting at 5 nm. Note: For each q value, large icons indicate values for the 15 nm film from the post-growth scan. The arrow indicates the direction of the increasing thickness. (b) Evolution of the peak position for each scattering feature with the increasing film thickness. Solid lines: FCC-indexed planes; dashed lines: HCP-indexed planes; and broad dashed lines: **q** values where both FCC and HCP planes can be indexed. The feature at $0.7\,\text{Å}^{-1}$ is the Pilatus intermodular gap, and the step at $1.1\,\text{Å}^{-1}$ is a shadow from the substrate shutter on the Be window. The arrow indicates the direction of the increasing thickness. (c) Extracted grain size (left) and strain (right, orange) from individual peak fitting and WH analysis. (d) Stacking fault probability calculated from Δq for each plane; green symbols are calculated relative to the feature at $1.3\,\text{Å}^{-1}$ and red symbols relative to the feature at $1.48\,\text{Å}^{-1}$.

values are consistent with the accumulation of several % stacking faults in FCC systems.[39]

According to Warren's selection rules,[40] stacking faults in FCC materials modify reflections in planes for which $h+k+l \neq 3m$. In the frame of an FCC lattice, it has been shown that shifts in the peak position and increased breadth (FWHM) of {220} peaks mark the onset of stacking faults along the close-packing direction.[21,24] In the case of powder-like samples, a Williamson-Hall (WH) plot can be a useful tool to decouple the influence of grain size and defects on shifts in scattering vector and line broadening. In a WH plot, $\Delta \boldsymbol{q}$ vs $\boldsymbol{q}$ across all peaks is fit to a linear or a quadratic function of the scattering vector using the Williamson-Hall (WH) relation[41] $\Delta q = 2\pi/D + 2\varepsilon q$, where the domain size D and lattice strain ε can be extracted from the intercept and slope of the plot, respectively. Figure 2(a) shows the WH plot for the film thickness starting at 5 nm, beyond which all three planes could be accurately fit to Gaussians. Despite only fitting three peaks [20 thickness values, linear least squares fitting with mean (μ) and standard deviation (σ) for the squared residuals R^2: $\mu = 0.84$ and $\sigma = 0.18$], linear fits consistently yield a non-zero positive intercept, indicating that part of the line broadening arises from small (~10 nm) grain scattering in the film [Fig. 2(c)]. The larger grain sizes extracted from the analysis below 8 nm thickness may reflect a greater extent of in-plane grain connectivity in the film, consistent with the larger q (and smaller island-island distance $D_{diffuse}$) at low thickness seen in Fig. 1(e). However, it is important to note that these grain sizes may also include contributions from changes in the peak breadth $\Delta \boldsymbol{q}$ and position $\boldsymbol{q}$, as both strain and grain size [Fig. 2(c)] are seen to exhibit similar changes below 8 nm film thickness where individual peaks only begin to emerge in the diffraction [Fig. 2(b)]. Additionally, fits of the data for films above 7 nm thickness converge towards a common slope, indicating a smaller role of microstrain on the observed $\boldsymbol{q}$-dependence of the line broadening away from the substrate.[42] As shown in Fig. 2(c), this strain decreases from as much as 5% when probing C_{60} within 7.5 nm of the substrate interface, to just under 2% in the upper 7.5 nm of the film away from the substrate. Previously reported strain values near the substrate interface using *in-situ* reflection high energy electron diffraction (RHEED) measurements of laser-deposited C_{60} on mica[43] yielded a value of ~3.2%, based on double lattice constant estimates. Given that amorphous glass is not expected to provide long-range templating for the C_{60} lattice, this extracted strain value is qualitatively in line with the powder-like growth observed herein (Fig. S5 in the supplementary material).

Because the *in-situ* measurements at this angle of incidence are most sensitive to the upper 7.5 nm of the film, in-plane scattering effectively captures both 1D line defects such as dislocations at grain boundaries between nanocrystals and 2D planar defects such as stacking faults within the 7.5 nm (~10 monolayer) cross-section of the nanocrystals. To compare the surface and bulk properties of the thin film, immediately after deposition, the substrate shutter was closed and the sample was probed between $\omega = 0°$ and 0.2° (Fig. S4 in the supplementary material). As observed during the *in-situ* measurements of the upper 7.5 nm layer, the $\{111\}_{FCC}$ peak exhibits a larger width and hence a smaller coherence length D than the other planes in the film. When the full film is measured along the horizon at a sample tilt $\omega = \theta_{c,glass} = 0.152°$, we find $D_{111} = 8.6$ nm, $D_{22L/300} = 4.9$ nm, and $D_{311} = 4.7$ nm, all consistent with those derived from the individual peak fitting of the *in-situ* data. The good fit ($R^2 = 0.999$) and negligible intercept suggest that a high degree of defects is the main cause for the $\boldsymbol{q}$-dependent peak broadening. The probability that the 4th plane in an FCC 111 plane sequence of the form A-B-C-A-B-C incorporates a planar fault of the form A-B-C-**B**-[…] is the stacking fault probability α, and the average number of planes between faults can be estimated as $1/\alpha$. The probability of deformation stacking faults α in a powder sample can be estimated using the Warren and Warekois formula,[44,45] which is given as

$$\alpha = \frac{\Delta(2\theta_{off})\pi^2 h_3}{j \tan\theta_{peak} \cos^2\varphi 270\sqrt{3}}, \tag{1}$$

where $\Delta(2\theta)$ is the peak offset in degrees, $h_3 = (h^2+k^2+l^2)/|h+k+l|$, j is the fraction of faulted planes for the family of planes $\{hkl\}$, θ_{peak} is the scattering angle of the reference peak, and $\cos\varphi$ is the average angle between the [111] plane and faulting planes within $\{hkl\}$. A closer examination of Fig. 2(b) (and Fig. S3 in the supplementary material) indicates that all three main peaks are shifted relative to their crystallographic references, and so, it is useful to compare *relative* shifts between two separate peaks, using the relation

$$\Delta 2\theta_{hkl} = G_{av} \cdot j \cdot \tan\theta \cdot \alpha, \tag{2}$$

where $\langle G_{av} \rangle = \pm 90\sqrt{3} \bullet h_3/\pi 2 l_0^2$, and h_3 is the reciprocal vector averaged over all faulting hkl planes given by $\langle \cos\varphi \rangle = h_3/\sqrt{3} l_0$. To estimate the stacking fault probability, the two diffraction features at 1.3 $Å^{-1}$ and 1.48 $Å^{-1}$ were referenced to the {220} and {311} planes, respectively. As shown in Fig. 2(d), the probability of deformation stacking faults in this film reaches a value of $\alpha = 68\%$ relative to the {220} planes and $\alpha = 4.2\%$ for the {311} planes as measured in the full 15 nm film. These values correspond to an average number of {111} planes between stacking faults relative to these references of 1.5 and 24 planes, respectively. The large calculated probabilities for the {220} planes below 7 nm are attributable to the significant uncertainty in the position of the scattering vector within the broad signal [*cf.* Fig. 2(b)]. As the film increases beyond $z_{1/e} = 7.5$ nm, the decreasing values of α are averaged-out with less influence from the substrate, with the plateau near ~12 nm, marking the measurement of just the upper "bulk" of the thin film. Although a full averaging out would be expected at $2z_{1/e} = 15$ nm, this difference may simply reflect the outsize influence of the 2 nm nearest the glass interface, where nucleation is taking place on the substrate. Although high for FCC metals, these values for α are consistent with simulations of stacking faults in vacuum-deposited C_{60} by Vaughan *et al.*[27] in which thin film samples were best described by models with a 50% probability of HCP stacking on FCC C_{60} underlayers.

Lastly, based on the *in-situ* and post-growth coherence lengths for the different reflections, it appears that once the C_{60} film transitions to steady state island growth, the

crystallites are limited to a size of roughly 10 nm along the FCC ⟨111⟩ and FCC ⟨22 L⟩/⟨300⟩ directions. However, the WH analysis for the full 15 nm film yields a larger grain size of 174 nm [square symbol, Fig. 2(c)], a factor 20 greater than the individual peaks and roughly 8× the 19.5 nm size calculated from AFM images (supplementary material, Table S1). This larger value arises from the fact that when probing the full film, the diffracted volume is a superposition of the microstructure through the vertical composition of the film. As seen in Fig. 2(a), both the measured peak position and width for the full film measurement are closer to the average values than the those of the upper half of the film. Moreover, comparison of the sizes obtained from integral breadth and WH analysis for the *in-situ* measurements and the full film [Fig. 2(c)] indicate close agreement between the two methods for all but the full film measurement, suggesting that the differences arise from the WH fitting of the full film data. Although the higher deposition rate, and short time interval between *in-situ* and post-deposition scans as compared to other studies suggest that dewetting might not be a main consideration for the observed grain size differences, combining this analysis with *in-situ* and post-deposition XRR as done by Bommel *et al.*[36] would facilitate a quantitative comparison between grain size distribution and film homogeneity normal to the surface, enabling a further link between the kinetics of film dewetting and as-grown film microstructure. Additionally, capturing a greater region of $\boldsymbol{q}$ space, *e.g.,* by probing at higher incident x-ray energy, would improve grain size estimates by using a greater number of diffraction orders in the analysis. It is well-documented that WH analyses can overestimate grain sizes by more than an order of magnitude,[42] in our specific case we can trace this inconsistency to the vertical inhomogeneity of the film, which is only resolved when comparing the analysis of the post-deposition and *in-situ* GIXS measurements.[46]

In summary, our results comprise *in-situ* monitoring of stacking fault evolution in C_{60} fullerene thin films while employing deposition rates consistent with scalable, state-of-the-art organic electronic device manufacturing. Although initial room-temperature growth on glass is marked by low roughness and nearly 6% in-plane microstrain, C_{60} quickly incorporates stacking faults, with $\alpha_{311} = 4.2\%$ and $\alpha_{220} = 68\%$. The observation that these material parameters vary with the distance from the substrate underscore the need for *in-situ* characterisation to understand the coupling of interfacial and bulk material properties in organic thin films. Our findings highlight the potential for *in-situ* GIXS as a powerful multi-length-scale probe for elucidating the structural and morphological evolution of vacuum-deposited molecular thin films for next-generation organic electronic devices.

See supplementary material for details on GIXS image reduction, *in-situ* lattice constant evolution, and post-deposition AFM analysis of the deposited thin film.

This work was supported by a Science and Technology Facilities Council (STFC) Challenge-Led Applied Systems Programme (CLASP, ST/L003309/1) focused on advancing the commercialization of organic solar cells. J.F.M.H. thanks Wolfson College, Oxford, for Junior Research Fellowship support. G.M. was supported by the Energy and Physical Sciences Research Council (EPSRC) Centre for Doctoral Training in New and Sustainable Photovoltaics and by the University College Oxford through the Oxford-Radcliffe scholarship. The authors thank G. Christoforo, P. R. Warren, S. V. Kesava, and H. Ye (Univ. of Oxford) and A. Warne and J. Rawle (Diamond Light Source) for their assistance with beamline instrumentation.

J.F.M.H. and M.R. developed the thin film research program. J.F.M.H. wrote the manuscript with contributions from all authors and directed the thin film characterisation and data analysis. I.R.R., G.M., and C.N. assisted with GIXS measurements and data analysis.

The authors declare no competing financial interests.

[1]W. Huang, J. Sinha, M.-L. Yeh, J. F. M. Hardigree, R. LeCover, K. Besar, A. M. Rule, P. N. Breysse, and H. E. Katz, Adv. Funct. Mater. **23**, 4094 (2013).
[2]L. Torsi, M. Magliulo, K. Manoli, and G. Palazzo, Chem. Soc. Rev. **42**, 8612 (2013).
[3]D. Di, A. S. Romanov, L. Yang, J. M. Richter, J. P. H. Rivett, S. Jones, T. H. Thomas, M. Abdi Jalebi, R. H. Friend, M. Linnolahti, M. Bochmann, and D. Credgington, Science **356**, 159 (2017).
[4]Heliatek GmbH, see https://www.heliatek.com/en/press/press-releases/details/heliatek-consolidates-its-technology-leadership-by-establishing-a-new-world-record-for-organic-solar-technology-with-a-cell-effi/ for "efficiency record press release."
[5]K. Myny, S. Steudel, S. Smout, P. Vicca, F. Furthner, B. van der Putten, A. K. Tripathi, G. H. Gelinck, J. Genoe, and W. Dehaene, Org. Electron. **11**, 1176 (2010).
[6]J.-H. Seo, T.-H. Chang, J. Lee, R. Sabo, W. Zhou, Z. Cai, S. Gong, and Z. Ma, Appl. Phys. Lett. **106**, 262101 (2015).
[7]S. Sharifzadeh, C. Y. Wong, H. Wu, B. L. Cotts, L. Kronik, N. S. Ginsberg, and J. B. Neaton, Adv. Funct. Mater. **25**, 2038 (2015).
[8]A. N. Brigeman, M. A. Fusella, Y. Yan, G. E. Purdum, Y.-L. Loo, B. P. Rand, and N. C. Giebink, Adv. Energy Mater. **6**, 1601001 (2016).
[9]R. R. Lunt, J. B. Benziger, and S. R. Forrest, Adv. Mater. **22**, 1233 (2010).
[10]O. V. Mikhnenko, P. W. M. Blom, and T.-Q. Nguyen, Energy Environ. Sci. **8**, 1867 (2015).
[11]M. A. Loi, E. da Como, F. Dinelli, M. Murgia, R. Zamboni, F. Biscarini, and M. Muccini, Nat. Mater. **4**, 81 (2004).
[12]G. E. Purdum, N. Yao, A. Woll, T. Gessner, R. T. Weitz, and Y.-L. Loo, Adv. Funct. Mater. **26**, 2357 (2016).
[13]O. D. Jurchescu, D. A. Mourey, S. Subramanian, S. R. Parkin, B. M. Vogel, J. E. Anthony, T. N. Jackson, and D. J. Gundlach, Phys. Rev. B **80**, 085201 (2009).
[14]Z. Kan, L. Colella, E. V. Canesi, A. Vorobiev, V. Skrypnychuk, G. Terraneo, D. R. Barbero, C. Bertarelli, R. C. I. MacKenzie, and P. E. Keivanidis, J. Mater. Chem. A **4**, 1195 (2016).
[15]E. Van Faassen and H. Kerp, Sens. Actuators B Chem. **88**, 329 (2003).
[16]C. Zhang, P. Chen, and W. Hu, Chem. Soc. Rev. **44**, 2087 (2015).
[17]A. Amassian, T. V. Desai, S. Kowarik, S. Hong, A. R. Woll, G. G. Malliaras, F. Schreiber, and J. R. Engstrom, J. Chem. Phys. **130**, 124701 (2009).
[18]A. R. Woll, T. V. Desai, and J. R. Engstrom, Phys. Rev. B **84**, 75479 (2011).
[19]S. Bommel, N. Kleppmann, C. Weber, H. Spranger, P. Schäfer, J. Novak, S. V. Roth, F. Schreiber, S. H. L. Klapp, and S. Kowarik, Nat. Commun. **5**, 5388 (2014).
[20]R. Banerjee, J. Novák, C. Frank, C. Lorch, A. Hinderhofer, A. Gerlach, and F. Schreiber, Phys. Rev. Lett. **110**, 185506 (2013).
[21]W. Krätschmer, L. D. Lamb, K. Fostiropoulos, and D. R. Huffman, Nature **347**, 354 (1990).
[22]J. Li, T. Mitsuki, M. Ozawa, H. Horiuichi, K. Kishio, K. Kitazawa, K. Kikuchi, and Y. Achiba, J. Cryst. Growth **143**, 58 (1994).
[23]S. Muto, G. V. Tendeloo, and S. Amelinckx, Philos. Mag. Part B **67**, 443 (1993).
[24]T. Ishiguro and Y. Hirotsu, Jpn. J. Appl. Phys., Part 1 **31**, L481 (1992).
[25]S.-H. Yoo, K. T. Butler, A. Soon, A. Abbas, J. M. Walls, and A. Walsh, Appl. Phys. Lett. **105**, 62104 (2014).
[26]Y. Nakayama, Y. Mizuno, T. Hosokai, T. Koganezawa, R. Tsuruta, A. Hinderhofer, A. Gerlach, K. Broch, V. Belova, H. Frank, M. Yamamoto, J. Niederhausen, H. Glowatzki, J. P. Rabe, N. Koch, H. Ishii, F. Schreiber, and N. Ueno, ACS Appl. Mater. Interfaces **8**, 13499 (2016).

[27]G. B. M. Vaughan, Y. Chabre, and D. Dubois, EPL Europhys. Lett. **31**, 525 (1995).
[28]C. Nicklin, J. F. Martinez Hardigree, A. Warne, S. Green, M. Burt, S. Lay, H. Shiers, M. Barnes, J. Naylor, A. Dorman, D. Wicks, S. Din, and M. Riede, Rev. Sci. Instrum. **88**, 103901 (2017).
[29]C. Uhrich, B. Männing, and G. Schwartz, (December 2010).
[30]J. Rivnay, S. C. B. Mannsfeld, C. E. Miller, A. Salleo, and M. F. Toney, Chem. Rev. **112**, 5488 (2012).
[31]A. Neuhold, J. Novák, H.-G. Flesch, A. Moser, T. Djuric, L. Grodd, S. Grigorian, U. Pietsch, and R. Resel, Nucl. Instrum. Methods Phys. Res., Sect. B **284**, 64 (2012).
[32]B. L. Henke, E. M. Gullikson, and J. C. Davis, At. Data Nucl. Data Tables **54**, 181 (1993).
[33]T. Schuettfort, L. Thomsen, and C. R. McNeill, J. Am. Chem. Soc. **135**, 1092 (2013).
[34]J. Filik, A. W. Ashton, P. C. Y. Chang, P. A. Chater, S. J. Day, M. Drakopoulos, M. W. Gerring, M. L. Hart, O. V. Magdysyuk, S. Michalik, A. Smith, C. C. Tang, N. J. Terrill, M. T. Wharmby, and H. Wilhelm, J. Appl. Crystallogr. **50**, 959 (2017).
[35]M. Schwartzkopf, A. Buffet, V. Körstgens, E. Metwalli, K. Schlage, G. Benecke, J. Perlich, M. Rawolle, A. Rothkirch, B. Heidmann, G. Herzog, P. Müller-Buschbaum, R. Röhlsberger, R. Gehrke, N. Stribeck, and S. V. Roth, Nanoscale **5**, 5053 (2013).
[36]S. Bommel, H. Spranger, C. Weber, N. Kleppmann, S. V. Roth, S. H. L. Klapp, and S. Kowarik, Phys. Status Solidi RRL **9**, 646 (2015).
[37]T. O'Haver, *A Pragmatic Introduction to Signal Processing* (University of Maryland at College Park, 2017).
[38]J. W. Eaton, D. Bateman, S. Hauberg, and R. Wehbring, *GNU Octave* (2017), see https://www.gnu.org/software/octave/.
[39]L. Balogh, G. Ribárik, and T. Ungár, J. Appl. Phys. **100**, 23512 (2006).
[40]B. E. Warren, Prog. Met. Phys. **8**, 147 (1959).
[41]G. K. Williamson and W. H. Hall, Acta Metall. **1**, 22 (1953).
[42]K. Santra, P. Chatterjee, and S. S. Gupta, Sol. Energy Mater. Sol. Cells **57**, 345 (1999).
[43]S. Yaginuma, K. Itaka, M. Haemori, M. Katayama, K. Ueno, T. Ohnishi, M. Lippmaa, Y. Matsumoto, and H. Koinuma, Appl. Phys. Express **1**, 15005 (2008).
[44]C. N. J. Wagner, Acta Metall. **5**, 427 (1957).
[45]B. E. Warren and E. P. Warekois, Acta Metall. **3**, 473 (1955).
[46]H. Savaloni, M. Gholipour-Shahraki, and M. A. Player, J. Phys. Appl. Phys. **39**, 2231 (2006).